

Supporting Information for

Tuning the plasmonic response up: Hollow cuboid metal nanostructures

Aziz Genç^{a,b,†}, Javier Patarroyo^{a,†}, Jordi Sancho-Parramon^{c,†}, Raul Arenal^{d,e}, Martial Duchamp^f,
Edgar E. Gonzalez^g, Luc Henrard^h, Neus G. Bastús^a, Rafal E. Dunin-Borkowski^f,
Victor F. Puentes^{a,i,j,*}, Jordi Arbiol^{a,j,*}

^a Catalan Institute of Nanoscience and Nanotechnology (ICN2), CSIC and The Barcelona Institute of Science and Technology (BIST), Campus UAB, Bellaterra, 08193 Barcelona, Catalonia, Spain.

^b Department of Metallurgy and Materials Engineering, Faculty of Engineering, Bartin University, 74100 Bartin, Turkey.

^c Rudjer Boskovic Institute, Zagreb, Croatia.

^d ARAID Fondation, 50018 Zaragoza, Aragon, Spain.

^e Laboratorio de Microscopias Avanzadas(LMA), Instituto de Nanociencia de Aragon (INA), Universidad de Zaragoza, 50018 Zaragoza, Spain.

^f Ernst Ruska-Centre for Microscopy and Spectroscopy with Electrons (ER-C) and Peter Grünberg Institute 5 (PGI-5), Forschungszentrum Jülich, D-52425 Jülich, Germany.

^g Geophysical Institute, Faculty of Engineering, Pontificia Universidad Javeriana and Nanoscale Science and Technology Centre, 110231, Bogota, Colombia.

^h Department of Physics. University of Namur. 61, rue de Bruxelles, 5000 Namur. Belgium.

ⁱ Vall d'Hebron Institut de Recerca (VHIR), 08035, Barcelona, Catalonia, Spain.

^j Institució Catalana de Recerca i Estudis Avançats (ICREA), 08010 Barcelona, Catalonia, Spain.

* Corresponding authors: victor.puentes@icn.cat, arbiol@icrea.cat.

† These authors contributed equally to this work.

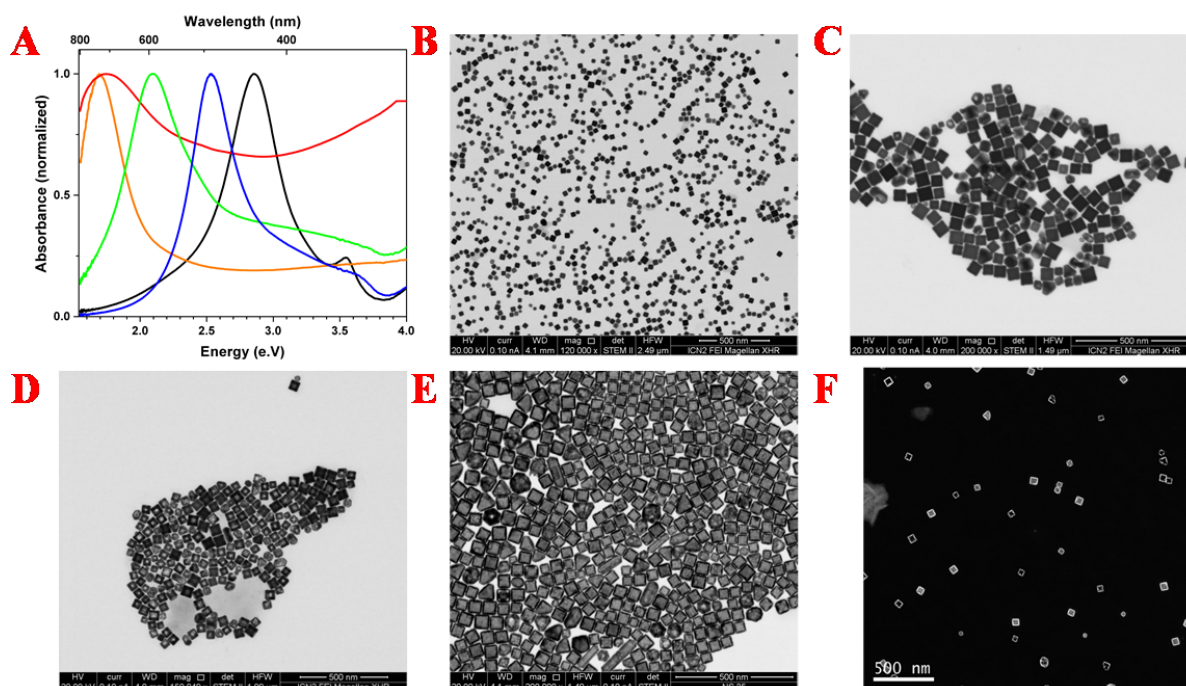


Figure S1. A. UV-Vis spectra of the solutions containing Ag nanocubes (in black), Ag@Au core-shell nanocubes (in blue), pinholed AuAg nanoboxes (in green), single-walled AuAg nanoboxes (in orange) and AuAg nanoframes (in red). Low magnification micrographs of the B. Ag nanocubes, C. Ag@Au core-shell nanocubes, D. pinholed AuAg nanoboxes, E. single-walled AuAg nanoboxes and F. AuAg nanoframes.

The shift of the plasmon resonances with the morphological modification is shown in Fig. S1A via bulk UV-Vis spectra obtained from respective solutions containing about 10^{12} NPs/mL. The concentration of Ag nanocubes and AuAg nanostructures are determined by measuring the amount of Ag nanocubes via Inductively Coupled Plasma-Mass Spectrometry (ICP-MS) and considering the size distributions measured by TEM. Low magnification micrographs of the 5 different nanostructures are also shown in Fig. S1B-S1F. The straightforward shift in the plasmon resonances of the Ag nanocubes, Ag@Au core-shell nanocubes, pinholed and single-

walled AuAg nanoboxes are observed in Fig. 1A. However, the UV-Vis spectrum of AuAg nanoframes showed rather wide peaks due to the low fraction of the nanoframes (~50% as stated in the Methods section and shown in Fig. 1F) in the solutions.

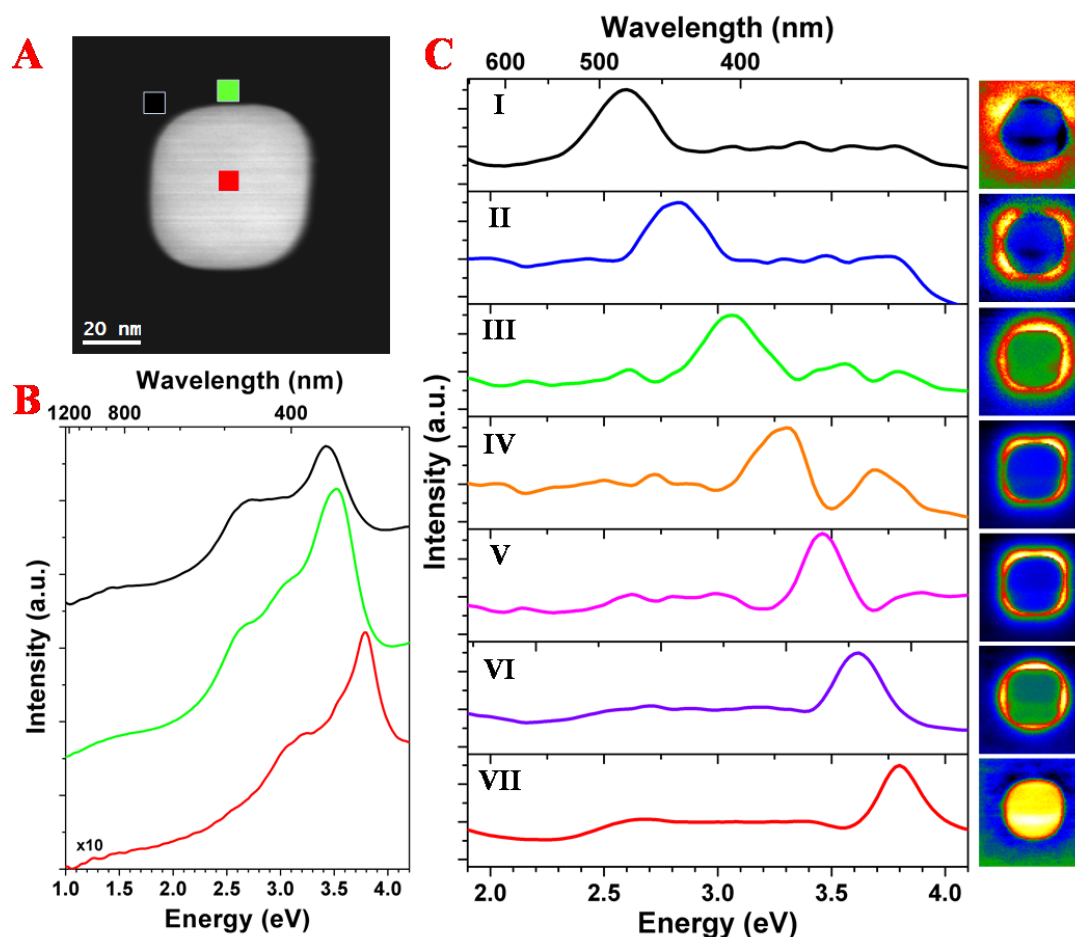


Figure S2. Plasmonic properties of the Ag nanocube. **A.** HAADF STEM micrograph of a 55 nm Ag nanocube with rounded corners. **B.** Selected area EEL spectra of the upper left corner, upper edge and bulk of the nanocube (areas are indicated in HAADF STEM micrograph, which are 5 pixel by 5 pixel). **C.** Spectra and abundance maps of 7 components obtained by VCA processing.

In Fig. S2A (also in Fig. 1B), an Ag nanocube (~55 nm in length) is shown. Zero-loss peak (ZLP) subtracted local EEL spectra obtained from the corner, edge and center of the nanocube are presented in Figure S2B, revealing the presence of several plasmon peaks located at ~2.6 eV, ~3.1 eV, ~3.4 eV, ~3.5 eV and ~3.8 eV. VCA processing shown in Figure S2C revealed the presence of 7 different components including the modes that can be related to the LSPR modes generated from the corners, edges and the bulk of the nanocube. As seen in the abundance maps of the corner modes (components #2, #4 and #5), the plasmon resonances are not confined at the corners but diffused through the edges, which is due to the fact that the nanocube has rounded corners, which surely affects the LSPR properties.^{1,2} This issue is further discussed on the basis of BEM simulations and presented in the supporting information section (see Fig. S3-S6).

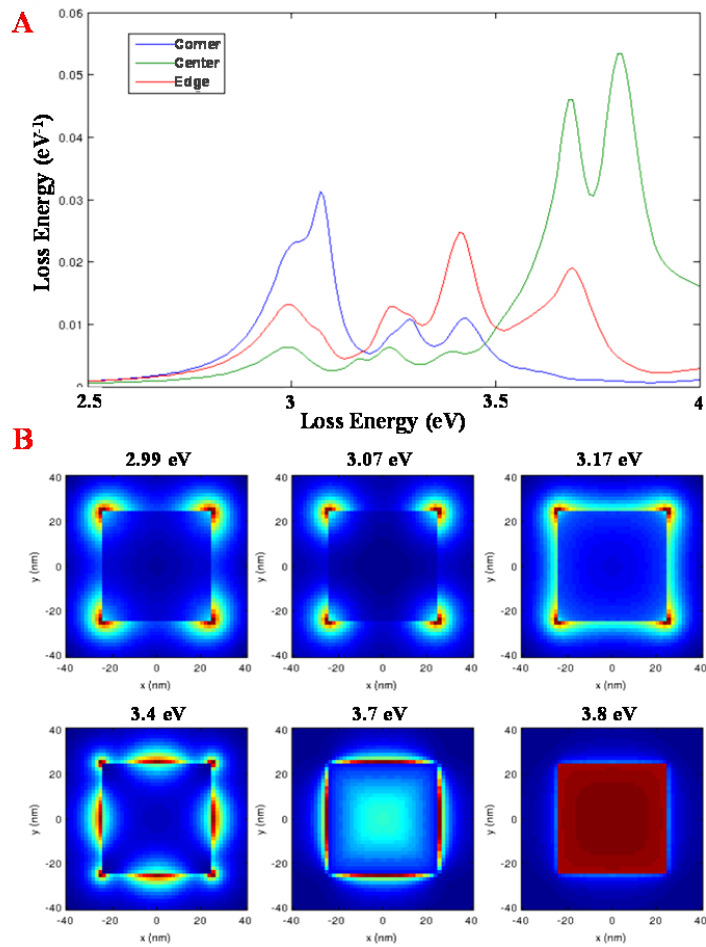


Figure S3. BEM simulated plasmonic properties of a 50 nm Ag nanocube standing in vacuum. **A.** Simulated selected area EEL spectra of the upper left corner, upper edge and bulk of the nanocube. **B.** Simulated plasmon distribution maps of 6 different modes located at 2.99 eV, 3.07 eV, 3.17 eV, 3.40 eV, 3.70 eV and 3.80 eV.

Figure 3 shows the BEM simulated plasmonic properties of a 50 nm Ag nanocube with sharp corners standing in vacuum. As discussed in the manuscript, plasmon resonances of the experimentally investigated Ag nanocube are not well confined at the corners and/or edges due to the fact that it has rounded corners. Ideal case with a perfect nanocube standing in vacuum

would generate plasmon resonances confined at the corners, edges end/or faces of the nanocube as shown in Fig. S3B.

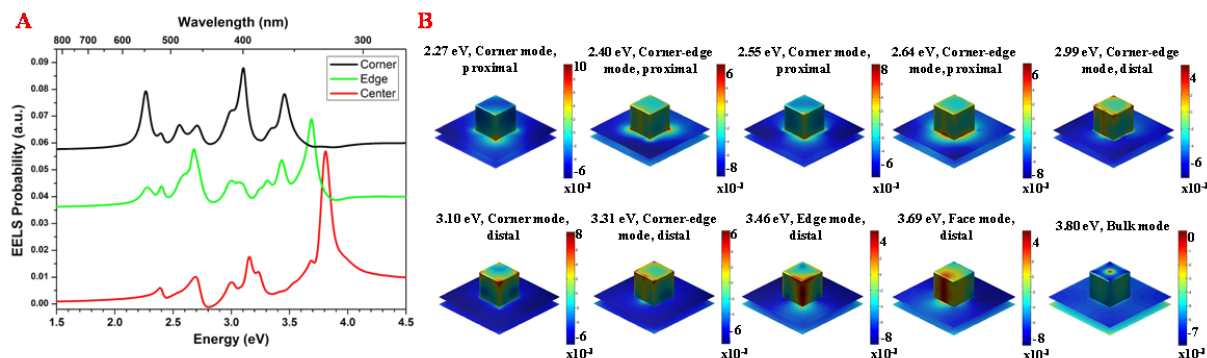


Figure S4. BEM simulated plasmonic properties of a 50 nm Ag nanocube standing on a 15 nm Si_3N_4 substrate. A. Simulated selected area EEL spectra of the upper left corner, upper edge and bulk of the nanocube. **B.** Simulated plasmon distribution maps (induced electric field intensity) of 10 different modes.

Another difference between the experimentally obtained Fig. S2 and simulated Fig. S3 is the presence of a substrate which also affects the plasmonic properties.^{3,4} Figure S4 shows the simulated plasmonic properties of a 50 nm Ag nanocube standing on a 15 nm Si_3N_4 substrate, which reveals the excitation of at least 4 additional plasmon modes compared to those excited from Ag nanocube standing in vacuum (Fig. S3). As the plasmon resonances of the nanocube interact with the substrate and hybridize³ various proximal (in contact with the substrate) and distal (not in contact with the substrate) modes are generated. In order to reveal the proximal and distal LSPR modes better, we have simulated the plasmon distribution maps, i.e., the induced electric field intensity, in 3D (Fig. S4B). It is also worth noting that plasmon resonances shifted

to lower energies and/or lower energy proximal modes are generated after the interaction with the substrate.

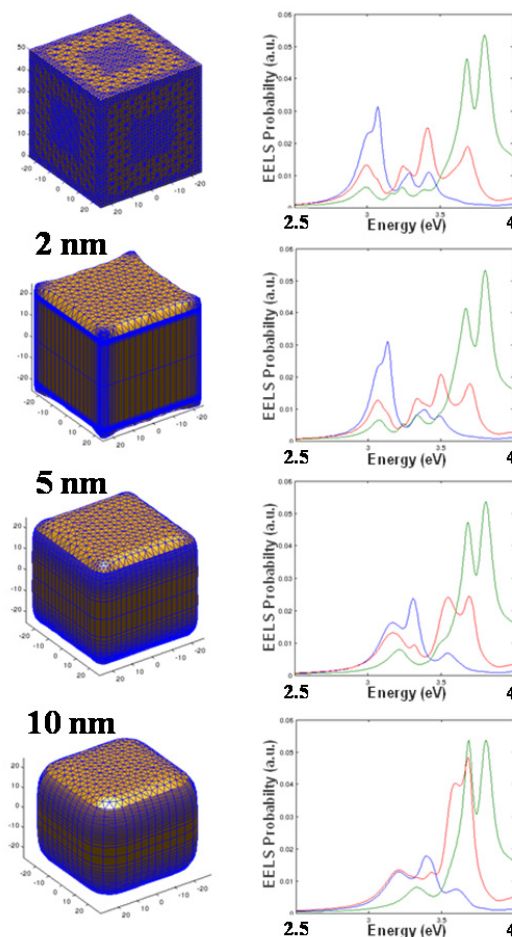


Figure S5. Effects of corner rounding on the plasmonic properties of Ag nanocubes. BEM simulated selected area EEL spectra of the corner (in blue), edge (in red) and bulk (in green) of Ag nanocubes (in vacuum) with perfect corners and corners rounded by 2 nm, 5 nm and 10 nm.

Figure S5 shows the effects of corner rounding on the plasmonic properties of Ag nanocubes (in vacuum), where BEM simulated local EEL spectra from the corner (in blue), edge (in red) and bulk (in green) of Ag nanocubes with perfect corners and corners rounded by 2 nm,

5 nm and 10 nm are presented. As the corner rounding increases, two main issues stand out: (i) localized surface plasmon resonances shift to higher energies and (ii) corner modes merge with edge modes and the edge modes merge with face modes.

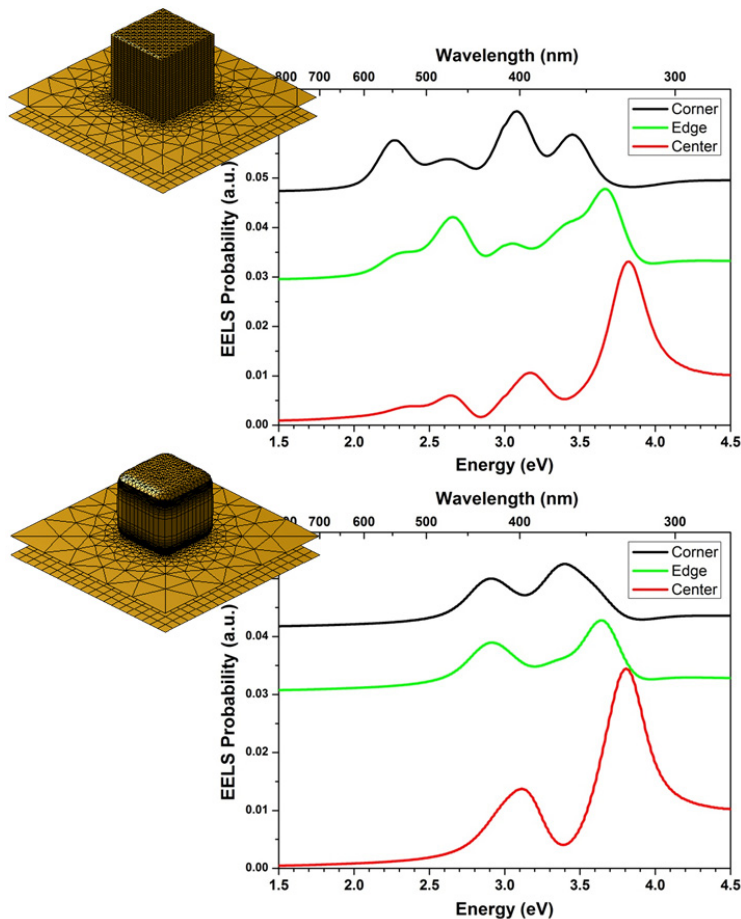


Figure S6. Comparison of plasmonic properties of Ag nanocubes with perfect and rounded corners. BEM simulated selected area EEL spectra of the corner (in black), edge (in green) and bulk (in red) of Ag nanocubes (on 15 nm thick Si_3N_4 substrates) with perfect corners and corners rounded by 15 nm.

With Figure S6, we summarize discussions on the effects of both the substrate and the corner rounding on the plasmonic properties. From the HAADF STEM micrograph presented in

Fig. S2A, we have assumed that the experimentally investigated Ag nanocube has corners rounded by about 15 nm. When we model such a nanocube on Si_3N_4 substrate, we can see an adequate qualitative agreement between the experimentally obtained EEL spectra (Fig. S2B) and BEM simulated EEL spectra (Fig. S6) is obtained. The simulated spectra are convoluted with a Gaussian profile, where each point is convoluted with a Gaussian function having a full width at half-maximum of 0.2 eV,⁵ in order to take into account the instrumental broadening and enable comparison with experimental data.

Figure S7 shows the HAADF STEM micrograph of a 51 nm Ag core – Au shell (more likely an AuAg alloy shell) core-shell nanocube and background subtracted local EEL spectra from different locations. Presence of wide peaks with several maxima are observed in these spectra, where it is noteworthy to point out that the EEL spectra obtained from the upper left corner and upper right corner are different from one another, suggesting the presence of some compositional differences between these corners. This issue is clearly revealed by the plasmon distribution maps obtained by VCA processing (5 different components and their abundance maps are shown in Fig. S7C) where the component #5 representing the bulk plasmon mode of Ag reveals that galvanic replacement reactions are not 100% homogeneous. By interpreting this plasmon map as an indication of Ag distribution, it can be seen that the upper right corner is corroded more than the other corners, resulting the presence of plasmon resonances at relatively lower energy of 2.3 eV which is confined mostly at the upper right corner.

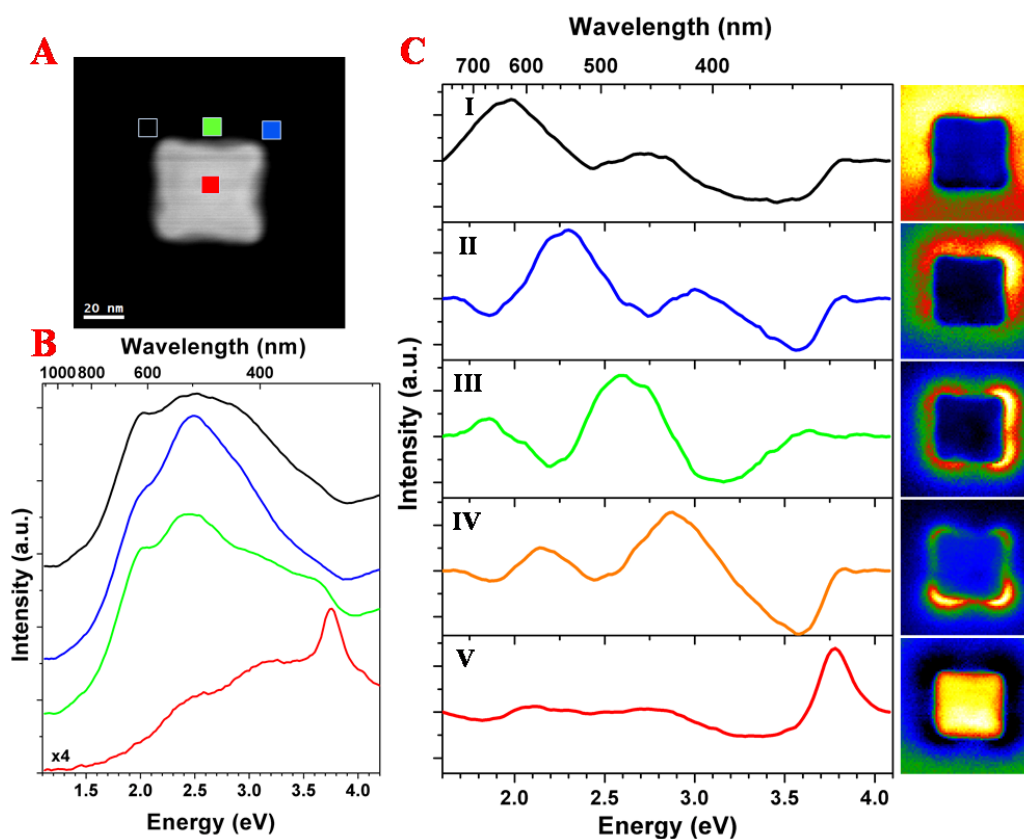


Figure S7. Plasmonic properties of the Ag-Au core-shell nanocube. **A.** HAADF STEM micrograph of a 51 nm AgAu core-shell nanocube. **B.** Selected area EEL spectra of the upper left and right corners, upper edge and bulk of the nanocube (areas are indicated in HAADF STEM micrograph, which are 5 pixel by 5 pixel). **C.** Spectra and abundance maps of 5 components obtained by VCA processing.

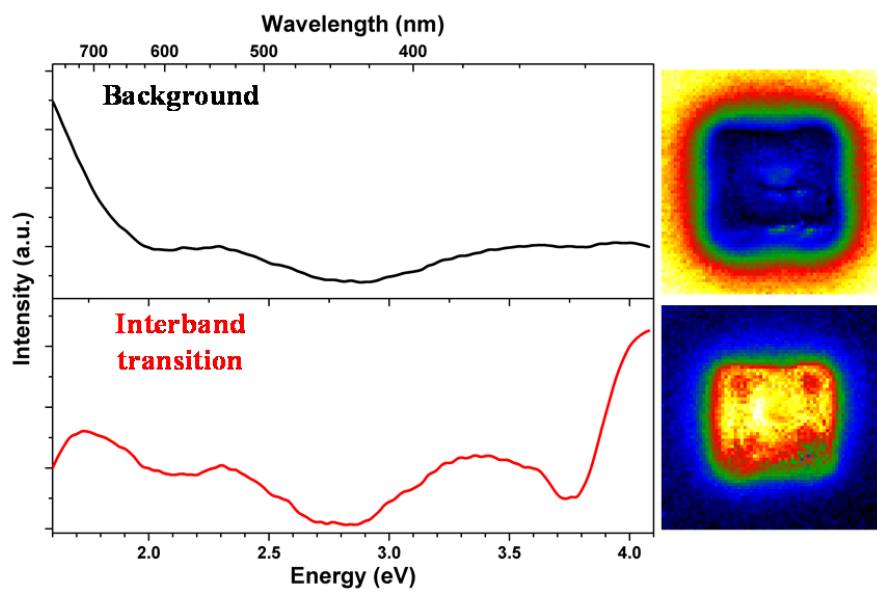


Figure S8. Spectra and abundance maps of the VCA components related to the background contribution and interband transitions for the pinholed AuAg nanobox.

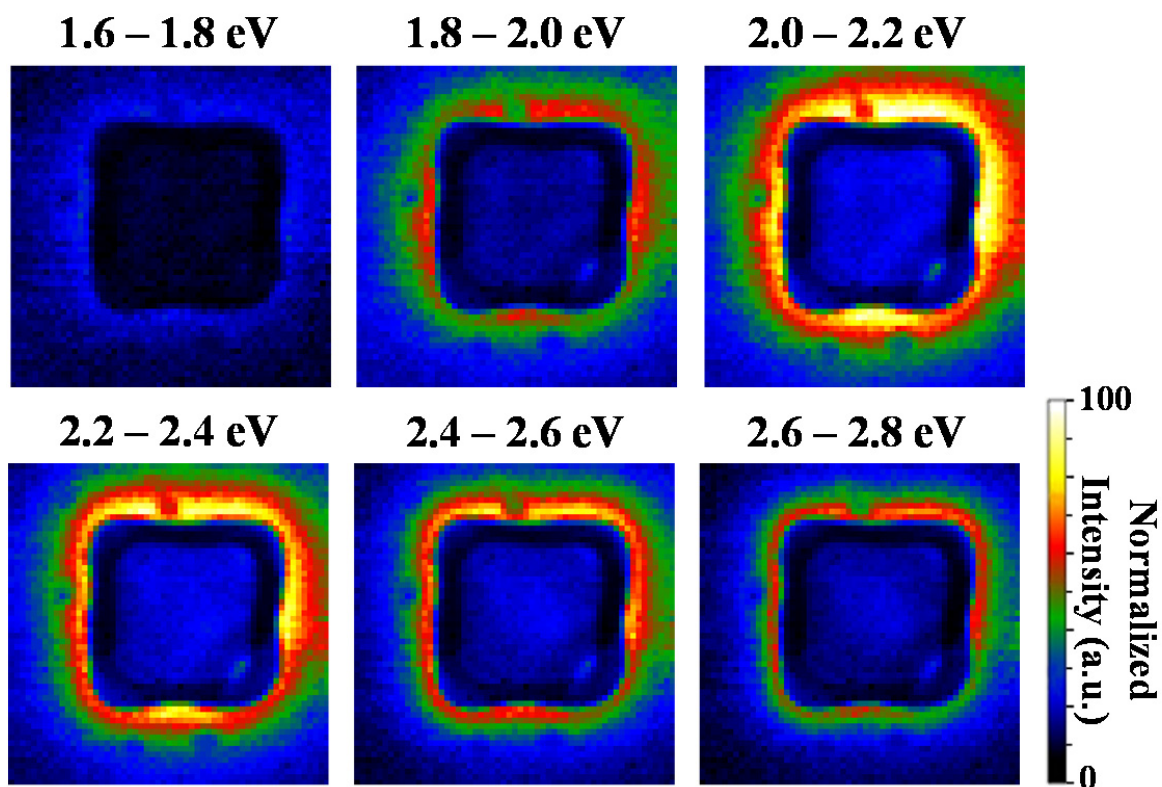


Figure S9. Distribution of plasmon intensities for the single-walled AuAg nanobox obtained by spectral filtering with a window of 0.2 eV. Plasmon distribution maps between 1.6 – 1.8 eV, 1.8 – 2.0 eV, 2.2 – 2.4 eV, 2.4 – 2.6 eV and 2.6 – 2.8 eV are presented, which confirms the homogeneous distribution of the plasmon resonances. Note that intensities of the plasmon maps are normalized to maximum and minimum values among all 6 maps.

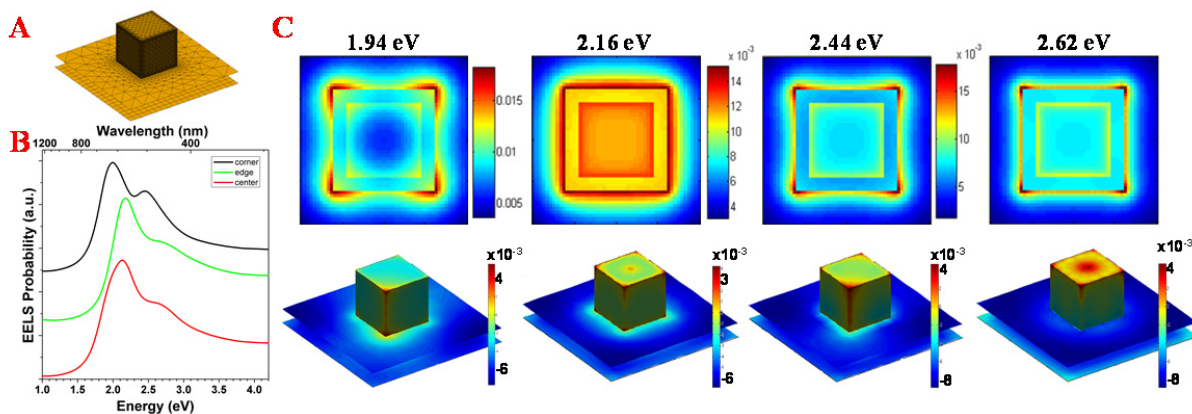


Figure S10. BEM simulations of the single-walled AuAg nanobox with sharp corners. A. Structural model used during simulations. **B.** Simulated local EEL spectra obtained from the corner, edge and center of the nanobox. **C.** Simulated plasmon maps of 4 different LSPR modes located at 1.94 eV, 2.16 eV, 2.44 eV and 2.62 eV along with their induced electric field intensity distribution maps in 3D (lower row).

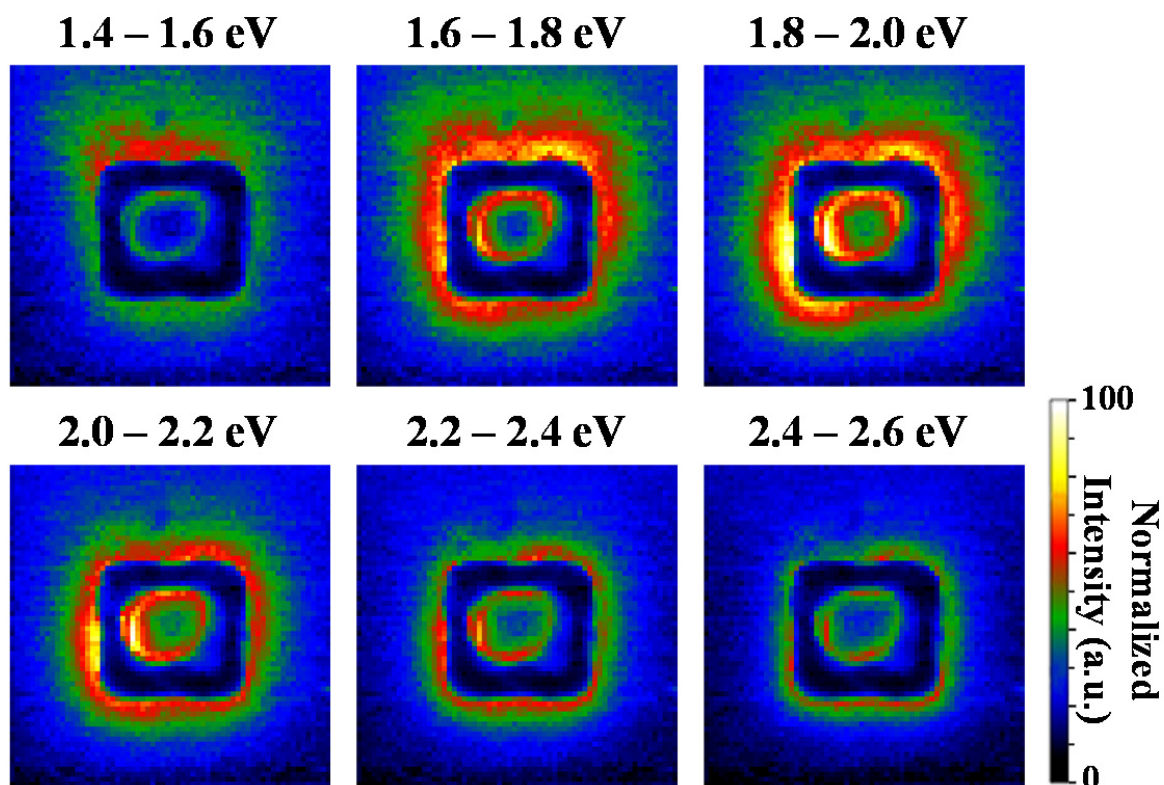


Figure S11. Distribution of plasmon intensities for the AuAg nanoframe obtained by spectral filtering with a window of 0.2 eV. Plasmon distribution maps between 1.4 – 1.6 eV, 1.6 – 1.8 eV, 1.8 – 2.0 eV, 2.2 – 2.4 eV and 2.4 – 2.6 eV are presented, confirming the homogeneous distribution of the plasmon resonances and interaction of the inner and outer resonances. Note that intensities of the plasmon maps are normalized to maximum and minimum values among all 6 maps.

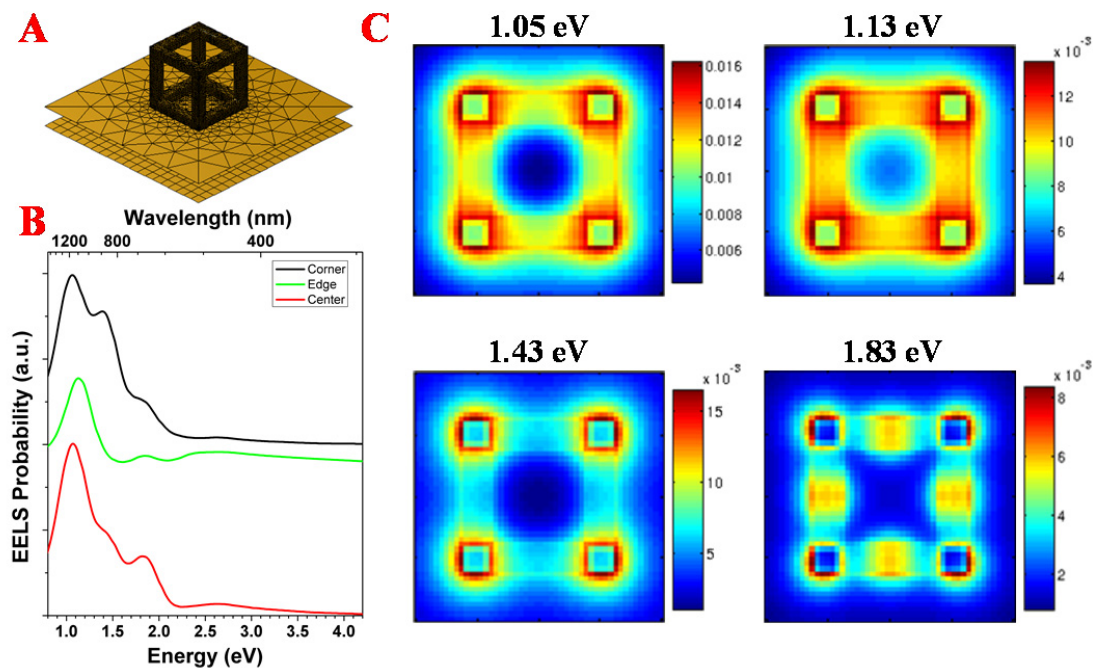


Figure S12. BEM simulations of the AuAg nanoframe with perfect corners and walls. **A.** Structural model used during simulations. **B.** Simulated local EEL spectra obtained from the corner, edge and center of the nanoframe. **C.** Simulated plasmon maps of 4 different LSPR modes located at 1.05 eV, 1.13 eV, 1.43 eV, and 1.83 eV

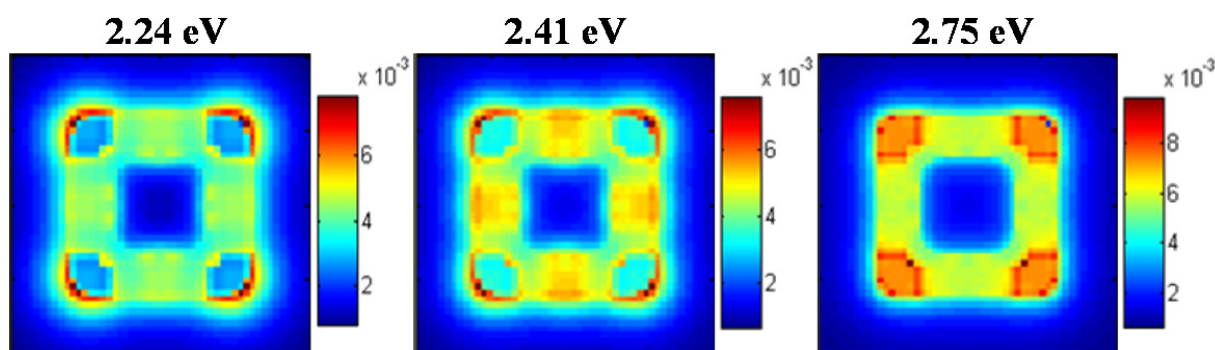


Figure S13. BEM simulations of the AuAg nanoframe. Simulated plasmon maps of 3 different LSPR modes located at 2.24 eV, 2.41 eV and 2.75 eV. These modes are higher energy modes of the simulated AuAg nanoframe and are complementary to Fig. 6 of the main text.

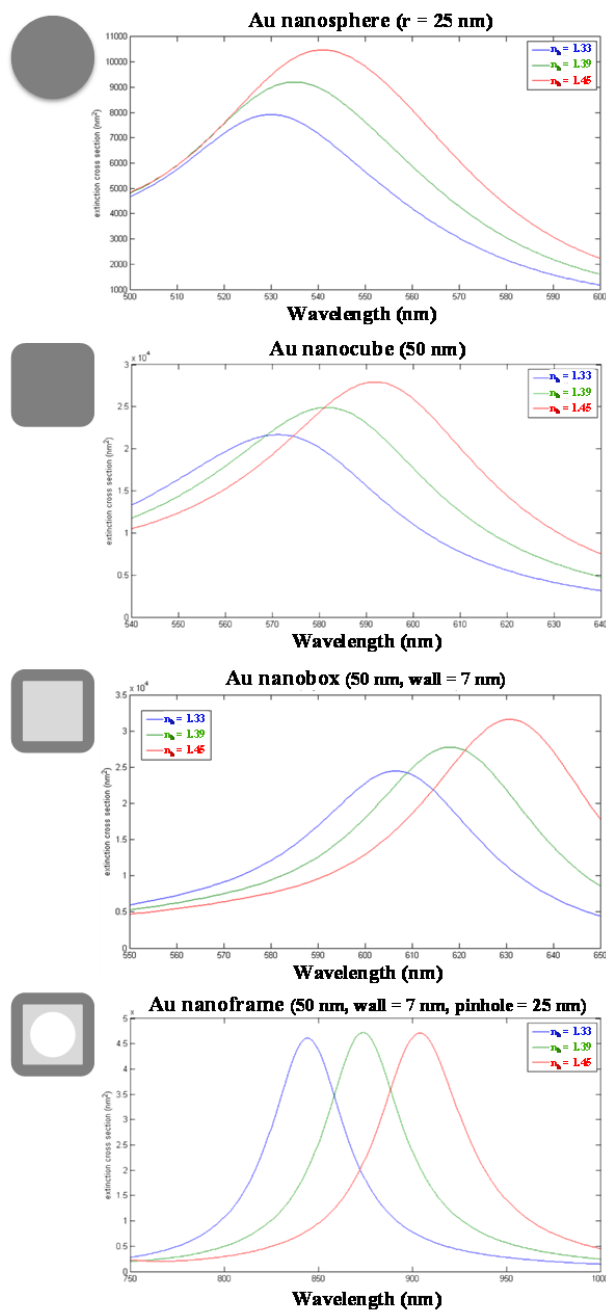


Figure S14. BEM simulated sensitivity of Au nanostructures. Sensitivity of spherical Au nanoparticles, Au nanocubes, Au nanoboxes and Au nanoframes, against the change in the surrounding medium. Blue spectra are in water with a refractive index $n = 1.33$, green spectra is an environment with a refractive index of $n = 1.39$, red spectra are the case for the medium with a refractive index of $n = 1.45$.

As stated in the main text, label-free optical sensing with plasmonic nanoparticles is based on the detection of adsorbate induced refractive index changes near or on the nanoparticles, which change the dielectric constant of the surrounding medium. Adsorbate induced shifts in LSPR can be expressed as $\Delta\lambda_{\max}$, which is simply equals to⁶:

$$\Delta\lambda_{\max} = \lambda_{\max} < \text{after} > - \lambda_{\max} < \text{before} >.$$

The sensitivity of plasmonic nanoparticles can be quantified by using the term sensitivity factor (SF), which is defined as the nanometers of shift in the LSPR peak of the nanoparticle per the refractive index unit (nm/RIU) of the surrounding medium.⁷ Thus, a higher SF depicts the generalization of larger shifts in the LSPR peak of the nanoparticle with smaller changes in the refractive index of the surrounding analytes.⁸

After experimentally obtaining an enhanced sensitivity with the hollow nanoboxes, we present the comparison of the sensitivities of different Au nanostructures such as 50 nm spherical Au nanoparticles, 50 nm Au nanocubes, 50 nm Au nanoboxes with 7 nm thick walls, 50 nm Au nanoframes with 7 nm walls and a spherical void ($R = 25$ nm) in each face, by using BEM simulations. It should be noted here that we have assumed rounded corners with a radii of 5 nm for the cuboid nanostructures in order to make them more realistic, as discussed in the present paper extensively. Sensitivity factors are highly dependent on the shape and composition of the nanostructures,⁷ for this reason we have used pure Au for all the nanostructures in order to study just the shape effects in sensitivity factors of different nanostructures. Figure S14 shows the BEM simulated UV-Vis spectra of the Au nanostructures in 3 different media. Since we have used nanoparticles in water to sense BSA conjugation events experimentally, we assumed a water ambient with a refractive index of $n = 1.33$, which is also used as reference and shown in blue lines. Then, we change the refractive index of the surrounding medium to keep track of the

shifts of LSPR peaks, where UV-Vis spectra shown with green and red lines are obtained by assuming media with refractive indexes of $n = 1.39$ and $n = 1.45$, respectively. In general, by just looking at the Fig. S14, one can see that Au nanoframes have the highest sensitivity to the changes in the environment whereas the spherical Au nanoparticles have the lowest among these nanostructures. More accurately, one can express these changes with the sensitivity factor (SF). BEM simulations revealed that Au spheres have a SF = 92 nm/RIU, Au nanocubes have a SF = 173 nm/RIU, Au nanoboxes have a SF = 204 nm/RIU and Au nanoframes have a SF = 495 nm/RIU. Higher sensitivity of the hollow nanostructures is not something unexpected as it is reported in the literature^{7,8,9} and shown experimentally here. However, it should be underlined here that the SF difference between Au nanocubes and Au nanoboxes, which have essentially the same outer surface area, are a lot lower than the values reported experimentally in the literature. For instance, Sun and Xia⁹ compared the sensitivity of Au nanospheres and nanoshells and reported that a SF of 60 nm/RIU measured for the solid nanosphere becomes 409 nm/RIU for the case of a hollow nanoshell of the same size, which corresponds to almost a 7 fold increase in the SF. Similarly, in their review article, Mahmoud et al.⁸ tabulated a 5 fold increased SF when comparing Au nanocubes and hollow Au nanocages. Such a discrepancy can have two main reasons, basically due to compositional and morphological differences. Firstly, the presence of Ag in the so-called hollow Au nanostructures may increase the SF of experimentally investigated hollow nanostructures since Ag is known to have better SF than Au.^{8,9} To check the effect of composition, we have simulated the response of 50 nm nanocubes composed of 60% Au and 40% Ag (similar to the composition of experimental nanoboxes) and obtained a SF of 181 nm/RIU, which is only 8 nm/RIU higher than the SF of pure Au nanocubes. We have also simulated the sensitivity of the AuAg nanoboxes composed of 60% Au and 40% Ag and found

that it is almost the same as the case of pure Au nanobox (SF= 204.2 nm/RIU). So, only the compositional differences cannot be accounted for the higher SF of the experimental hollow nanoparticles. Synthesized hollow nanoshells, nanoboxes or nanocages are known to have multiple voids on the faces.^{8,10,11} Yet, hollow nanoboxes are simulated as having intact walls. The presence of voids along the nanostructures would increase the surface area of the nanostructures and thereby increase the sensitivity, explaining the discrepancy shown before between experimental and simulated results.

REFERENCES

- (1) Grillet, N.; Manchon, D.; Bertorelle, F.; Bonnet, C.; Broyer, M.; Cottancin, E.; Lerme, J.; Hillenkamp, M.; Pellarin, M. Plasmon coupling in silver nanocube dimers: Resonance splitting induced by edge rounding. *ACS Nano* **2011**, *5*, 9450-9462.
- (2) McMahon, J.M.; Wang, Y.; Sherry, L.J.; Van Duyne, R.P.; Marks, L.D.; Gray, S.K.; Schatz, G.C. Correlating the Structure, Optical Spectra, and Electrodynamics of Single Silver Nanocubes. *J. Phys. Chem. C* **2009**, *113*, 2731-2735.
- (3) Zhang, S.; Bao, K.; Halas, N.J.; Xu, H.; Nordlander, P. Substrate-induced Fano resonances of a plasmonic nanocube: A route to increased-sensitivity localized surface plasmon resonance sensors revealed. *Nano Letters* **2011**, *11*, 1657-1663.
- (4) Nicoletti, O.; de la Peña, F.; Leary, R.K.; Holland, D.J.; Ducatti, C.; Midgley, P.A. Three-dimensional imaging of localized surface plasmon resonances of metal nanoparticles. *Nature* **2013**, *502*, 80–84.
- (5) Bigelow, N.W.; Vaschillo, A.; Iberi, V.; Camden, J.P.; Masiello, D.J. Characterization of the Electron- and Photon-Driven Plasmonic Excitations of Metal Nanorods, *ACS Nano*, **2012**, *6*, 7497–7504.
- (6) Zhao, J.; Zhang, X.; Yonzon, C.R.; Haes, A.J.; Van Duyne, R.P. Localized surface plasmon resonance biosensors. *Nanomedicine* **2006**, *1*, 219-228.
- (7) Mayer, K.M.; Hafner, J.H. Localized surface plasmon resonance sensors. *Chemical Reviews* **2011**, *111*, 3828-3857.
- (8) Mahmoud, M.A.; O'Neil, D.; El-Sayed M.A. Hollow and Solid Nanoparticles in Sensing and in Nanocatalysis. *Chem. Mater.* **2014**, *26*, 44–58.

(9) Sun, Y.; Xia, Y. Increased sensitivity of surface plasmon resonance of gold nanoshells compared to that of gold solid colloids in response to environmental changes. *Anal. Chem.* **2002**, *74*, 5297-5305.

(10) Wiley, B.; Sun, Y.; Chen, J.; Cang, H.; Li, Z.Y.; Li, X.; Xia, Y. Shape-Controlled Synthesis of Silver and Gold Nanostructures. *MRS Bulletin* **2005**, *30*, 356-361.

(11) González, E.; Arbiol, J.; Puntès, V. F. Carving at the Nanoscale: Sequential Galvanic Exchange and Kirkendall Growth at Room Temperature. *Science* **2011**, *334*, 1377-1380.